Improved Strength–Ductility Synergy of a CoCrNi Medium-Entropy Alloy by Ex Situ TiN Nanoparticles

Anjing Wang, Jianying Wang, Feipeng Yang, Tao Wen, Hailin Yang,* and Shouxun Ji*

The introduction of ex situ reinforcement particles to increase the strength of alloys generally reduces ductility. Herein, a method to fabricate CoCrNi/TiN composite via spark plasma sintering (SPS) and rolling and annealing to achieve a superior combination of strength and ductility is presented. Under the as-SPSed condition, the CoCrNi/TiN composites exhibit the fracture strain of 41.9%, yield strength (YS) of 0.48 GPa, ultimate tensile strength (UTS) of 0.88 GPa, and hardness of 232.0 Hv. After rolling at 25 °C for the thickness reduction of 50%, the alloy presents fracture strain of 6.9%, YS of 1.24 GPa, UTS of 1.41 GPa, and hardness (408.9 Hv). After rolling at 25 °C for the thickness reduction of 50%, and annealing at 700 °C for 1 h, a good combination of YS of 0.77 GPa, UTS of 1.01 GPa, and fractured strain of 55.2% can be obtained in the samples. The superior strength–ductility synergy can be attributed to the refined structure, the formation of lattices defects (i.e., stacking faults [SFs] and Lomer–Cottrell Locks (LCs)), the interaction of nanotwin–TiN particles, and the concurrent process of potential grain boundary sliding accommodated by intragranular dislocation in the softer face-centered cubic (fcc) matrix.

1. Introduction

Metallic materials with strength–ductility synergy are highly desired in many key engineering applications, such as the overhead cable or integrated circuit frameworks in high-speed trains. The simultaneous improvement in strength and ductility has been a major challenge in materials development over decades. Currently, the CoCrNi medium-entropy alloy (MEA) with exceptional ductility and nondesirable strength at room and cryogenic environments has drawn much attention,[1–6] and it is very suitable for defect engineering studies through its low stacking fault energy (SFE). Various defect strengthening mechanisms were employed to improve the strength of CoCrNi alloy with a simple face-centered cubic (fcc) crystal structure, including point defects (C/B/Al/Mo atoms[7–10]), linear defects (dislocations[11]), interface defects (grain boundaries,[2,12,13] twin boundaries,[6,14,15] SFs,[16] LCs,[17] and short-range order[8,18]), and volume defects (ex situ particles,[19,20] in situ precipitates,[9,16] and fcc–hexagonal close packed phase transformation[11,18,21]). Regrettably, these can strengthen the CoCrNi MEA but often decrease or even bankrupt the ductility.[22]

Grain refinement is a powerful method to overcome the trade-off of strength and ductility.[13,23,24] Integration of severe plastic deformation (SPD) and suitable postmortem annealing was useful to relax stress and lattice defects and deliver outstanding mechanical properties.[23,24] Ex situ and in situ particles that provide a strong resistance between two neighboring grains/subgrains or act as inoculations and nucleation sites also deliver fine grain sizes.[9,13,25,26] However, particles that do not have a coherent orientation relationship with matrix impart a reduction of ductility and fracture toughness as stress concentration increases,[19,27] and particles that have a coherent OR with matrix can codeform in concert with the matrix via dislocation transmissions across reinforcing units, which lead to a superior combination of mechanical properties.[28–30] In addition, the occurrence of grain boundary sliding (GBS) that promotes grain rotation and eliminates orientation relationship between matrix and ex situ/in situ phases can accommodate large plastic deformation and achieve excellent ductility.[30,31] For instance, the elimination of orientation relationship between fcc and B2 phases through GBS during tensile testing and the generation of geometrically necessary dislocations (GNDs) in soft fcc matrix can accommodate plastic deformation effectively.[32] These allow the $Al_9(CoCrFeMnNi)_{91}$ alloy to offer super plasticity elongation of 2000%.[30] This phenomenon and mechanism should be applied to other systems.

Therefore, this work aims to explore a feasible processing route to obtain the CoCrNi/TiN composites with significantly improved strength and ductility. The CoCrNi/TiN powder was prepared via a novel coating method, and CoCrNi/TiN composites were synthesized using the combination of spark plasma sintering (SPS), several deformation, and postmortem annealing. The effects of

A. Wang, J. Wang, F. Yang, T. Wen, H. Yang
State Key Laboratory of Powder Metallurgy
Central South University
Changsha 410083, China
E-mail: y-hailin@csu.edu.cn

S. Ji
Brunel Centre for Advanced Solidification Technology (BCAST)
Brunel University London
Uxbridge, Middlesex UB8 3PH, UK
E-mail: shouxun.ji@brunel.ac.uk

The ORCID identification number(s) for the author(s) of this article can be found under https://doi.org/10.1002/adem.202200939.

thermomechanical treatments on the microstructure (including grain size, lattice defects, orientation relationship between matrix and TiN particles) and mechanical performance were studied. Furthermore, the corresponding strengthening mechanisms for synthesized CoCrNi/TiN composite were discussed.

2. Experimental Section

2.1. Powder and Materials Fabrication

Commercial TiN nanoparticles (Shuitian, Shanghai, China, ≈ 40 nm) and the CoCrNi prealloyed powder (Made in house, 15–53 μm) were applied as the raw materials. The CoCrNi/TiN powder was mixed and the preparation of composite (volume fraction of TiN, 1%) is schematically shown in **Figure 1**a. TiN nanoparticles were first dissolved into the alcohol with 0.75 wt.% $(CH_3)_4NOH$ as dispersant. The CoCrNi prealloy powder was subsequent introduced to produce CoCrNi/TiN suspension through stirring at 60 °C. The mixed powder was then transferred to a vacuum oven (60 °C for 24 h). Detailed morphologies of the CoCrNi powder and the CoCrNi/TiN mixed powder are listed in Figure 1b,c. The majority of raw powder exhibited a spherical morphology and TiN nanoparticles were homogeneously distributed on the surface of CoCrNi powder. In comparison with conventional methods, including dry milling and wet milling in alcohol,[33–35] the key advantage of the present method is that the CoCrNi powder showed no change in morphologies after coating.

After coating, the CoCrNi/TiN powder mixture was consolidated via SPS in the graphite die at 1080 °C. During SPS, constant pressure and heating rate was fixed at 40 MPa and 100 °C min^{-1}, respectively. SPSed samples size was 40 mm in diameter and 8 mm in height. Rolling process was subsequently performed at 25 °C to a thickness of 4 mm, followed by annealing at 700 °C for 1 h.

2.2. Microstructure Characterization

Microstructural evolution was characterized via various electron microscopes. Scanning electron microscope (SEM) and electron backscattered diffraction (EBSD) equipped with the TSL OIM data analysis software were performed in a FIB Helios NanoLab G3 UC SEM. To investigate deformation mechanisms, we further characterized the detailed microstructures with transmission electron microscopy (TEM; Tecnai G2 60-300).

2.3. Mechanical Testing

Dog-bone-shaped tensile sample with a gauge length of 12.5 mm and cross section of 3.2×1.4 mm^2 was fabricated via electrical discharge machining. Uniaxial tensile tests were performed at room temperature (20 °C) using an MTS Alliance RT30 mechanical testing system. Vickers hardness was detected via an ASTM E 384-08 hardness tester. The load and time were set to be 300 g and 10 s, respectively.
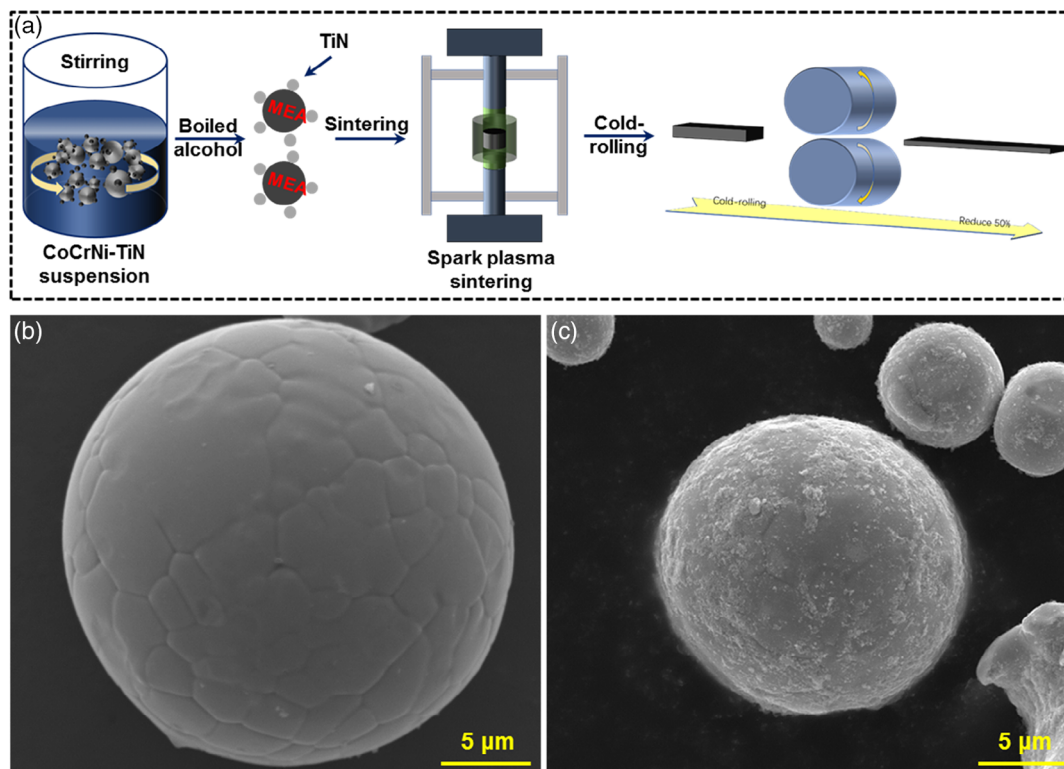

Figure 1. a) Schematic diagram of synthesis procedure for the CoCrNi/TiN mixed powders and the CoCrNi/TiN composites. SEM image indicating the morphology of b) the CoCrNi powder and c) the CoCrNi/TiN mixed powder.
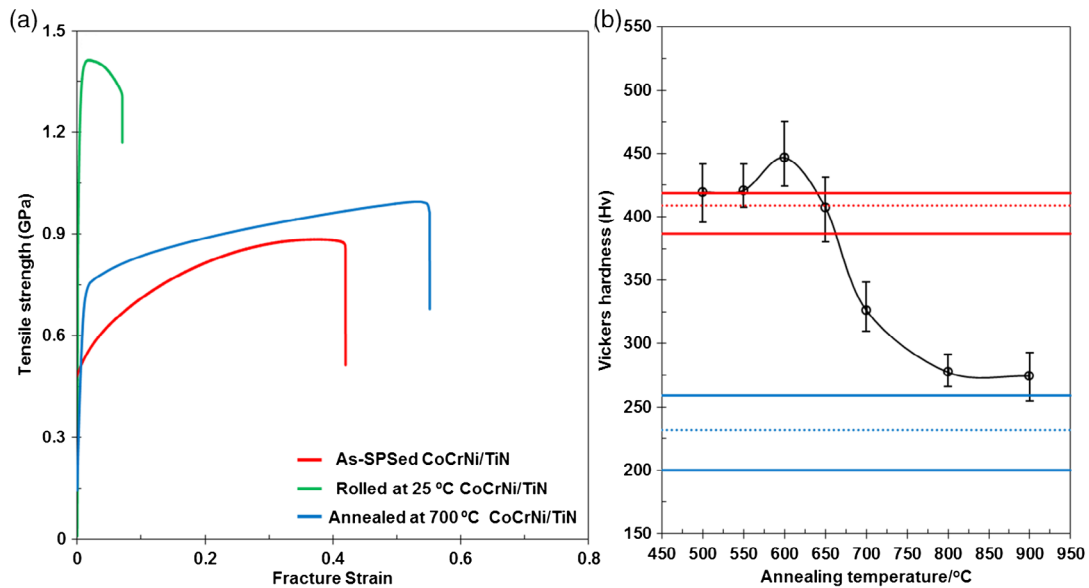
Figure 2. a) The engineering tensile stress–strain curves and b) the hardness of the CoCrNi/TiN composites under different temperatures with 1 h annealing.

3. Results and Discussion

The engineering tensile stress–strain curves of the CoCrNi/TiN composites are displayed in **Figure 2**a, and the corresponding values are summarized in **Table 1**. It is indicated that that the YS, UTS, and fractured strain (FS) of the as-SPSed CoCrNi/TiN composites were 0.48 GPa, 0.88 GPa, and 41.9%, respectively. After rolling at 25 °C for a thickness reduction of 50%, the YS increased to 1.24 GPa, UTS increased to

1.41 GPa, and FS reduced to 6.9%. With subsequent annealing at 700 °C for 1 h, the YS was 0.77 GPa, the UTS was 1.01 GPa, and the FS was 55.2%. Clearly, the mechanical response of the CoCrNi/TiN composites was manipulated through different processing methods. Cold rolling with annealing could provide a superior strength–ductility synergy.

The hardness of the CoCrNi/TiN composites with various conditions is presented in Figure 2b. The hardness of as-SPSed composites varied between 200.1 and 258.9 Hv. The hardness of composites was increased significantly after rolling process, reaching up to values between 386.84 and 418.86 Hv. The hardness improved initially with increasing annealing temperatures, peaking at 446.6 Hv at 600 °C from 418.9 Hv at 500 °C, followed by a gradual decrease to 274.4 Hv at 900 °C.

EBSD maps of the CoCrNi/TiN composites under various conditions are shown in **Figure 3**. The heterogeneous matrix grains were detected in four sets of samples. The as-SPSed samples had the largest coarse grains (average grain size of 11.4 μm), with low number density of microscale twins observed in
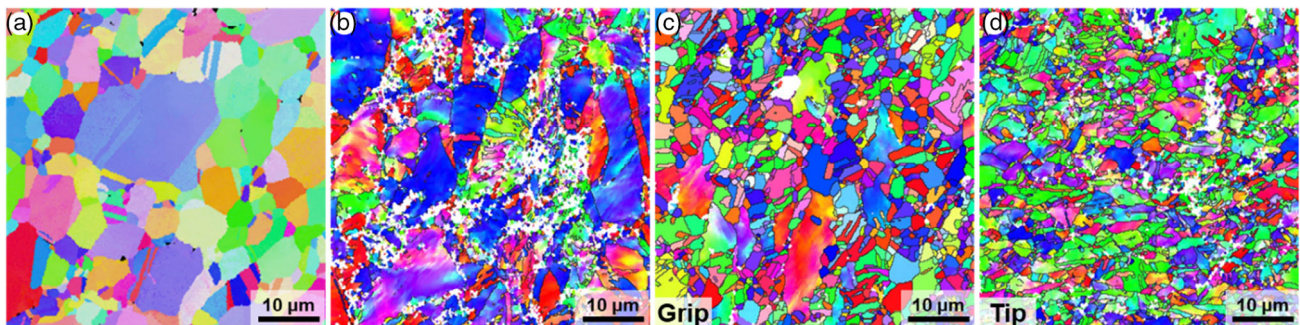
Table 1. The YS, UTS, FS, and hardness of the composites with various conditions.

Treatment	YS [GPa]	UTS [GPa]	FS [%]	Hardness [HV]
As SPSed	0.48	0.88	41.9	232.0
Rolling for 50% thickness reduction	1.24	1.41	6.9	408.9
Rolling for 50% thickness reduction +annealing at 700 °C for 1 h	0.77	1.01	55.2	326.4

Figure 3. EBSD–inverse pole figures (IPFs) of the CoCrNi/TiN composites under various conditions: a) as-SPSed; b) rolling treatment; positions of c) grip and d) tip of tensile test samples with rolling and annealing treatment.

**ADVANCED
SCIENCE NEWS**

www.advancedsciencenews.com

**ADVANCED
ENGINEERING
MATERIALS**

www.aem-journal.com

Figure 3a. The highly elongated grains could be detected in the composites after the rolling process, as shown in Figure 3b. Moreover, fine recrystallization grains were detected after annealing at 700 °C. The average grain sizes of the positions of grip and tip are 2.06 μm (Figure 3c) and 1.74 μm (Figure 3d), respectively. Also, obvious lattice distortion can be observed in the position of tip in counterpart with the position of grip. Annealing treatment also brought high-angle grain boundaries (misorientation >15°: **Figure 4**). The misorientation angles appeared strongly at 60°, suggesting that more annealing twins were formed under annealing at 700 °C.

The FS of the composites under different conditions is depicted in **Figure 5**. The dimple-like structures were detected in three sets of tensile samples. In addition, a few elongated voids were also detected in the FS of the rolled samples. These confirm that ductile fractures exist in the as-SPSed and annealed composites.

It is clear in Figure 2 that annealing at 700 °C delivers a good strength–ductility synergy (YS of 0.77 GPa, UTS of
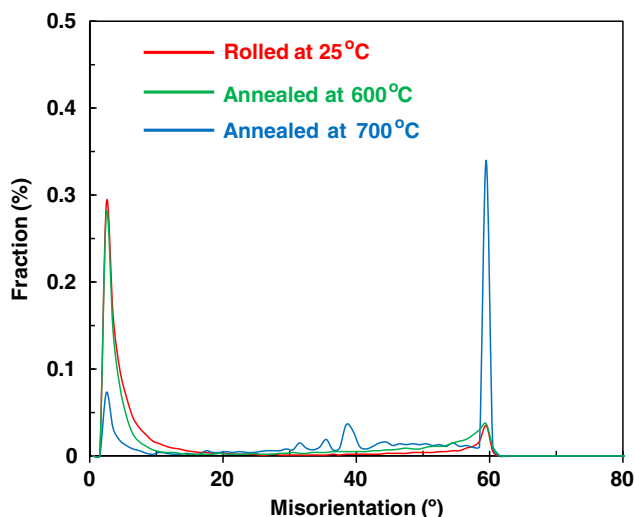
1.01 GPa, and hardness of 326.4 Hv) and ductility (FS of 55.2%). Correspondingly, the detailed TEM investigation at the grip of tensile CoCrNi/TiN composites after annealing at 700 °C is shown in **Figure 6**a,b. High-resolution (HR) TEM images (Figure 6b) and selected-area electron diffraction (SAED) pattern (L1) from the interface of fcc matrix and TiN phases indicated that fcc matrix was taken along [011] direction, with an interplanar spacing of 0.176 nm for $(200)_{fcc}$ plane, and TiN phase was taken along [013] direction, with an interplanar spacing of 0.215 nm for $(200)_{TiN}$ plane. Moreover, a semicoherent interface (misfit angle θ: 9.1°) can be identified together with a high number density of misfit dislocations. Meanwhile, the detailed TEM investigation of the tip of tensile CoCrNi/TiN composites after annealing at 700 °C is shown in Figure 6c–i. The existence of Orowan's effect induced by the interaction between mobile dislocations and TiN nanoparticles could be detected in the bright field transmission electron microscopy image of Figure 6c. The generation of the high dislocation density was also detected within fcc matrix grains (Figure 6d), which suggested the role of intragranular dislocations for the accommodation of plastic deformation during the plasticity test. In addition, maintaining relatively small size and near-equiaxed morphology during the plasticity test confirmed the occurrence of grain boundaries sliding (see EBSD results in Figure 6d).[36] Moreover, there was no specific orientation relationship between fcc matrix and TiN phases at the tip of samples, as indicated in the HRTEM image of Figure 6e and SAED pattern of L2. Elimination of the orientation relationship between matrix and some TiN phases through the occurrence of potential GBS might accommodate grain rotation during the plasticity test in this study.

Meanwhile, the interaction between nanotwins (about 10 nm) and TiN nanoparticles distributed at grain boundary was also detected in the BFTEM image of Figure 6f. The indexed SAED pattern L3 and HRTEM image (L3) identified the presence of twins. The TiN particles were also embedded in the nanotwins with a larger thickness–length ratio, as shown in Figure 6g. Liu et al. result showed that the effective critical resolved shear stress (CRSS) of twin growth is linear with the volume fraction and aspect ratio of embedded particles.[37] Twins did not grow after annealing at 700 °C, which might be related to the increase in CRSS induced by embedded TiN particles. The nanotwins could
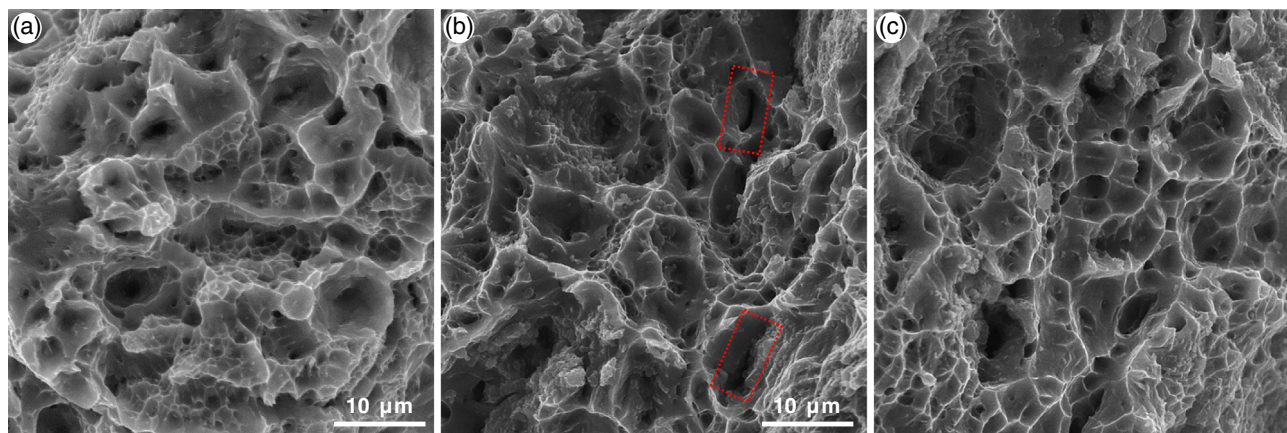

Figure 4. The misorientation angle distributions of the composite under various conditions, including rolling, rolling with annealing at 600 °C for 1 h, and rolling with annealing at 700 °C.

Figure 5. The fractured morphologies of CoCrNi/TiN composites treated by a) SPS, b) rolling, and c) rolling + annealing at 700 °C for 1 h.
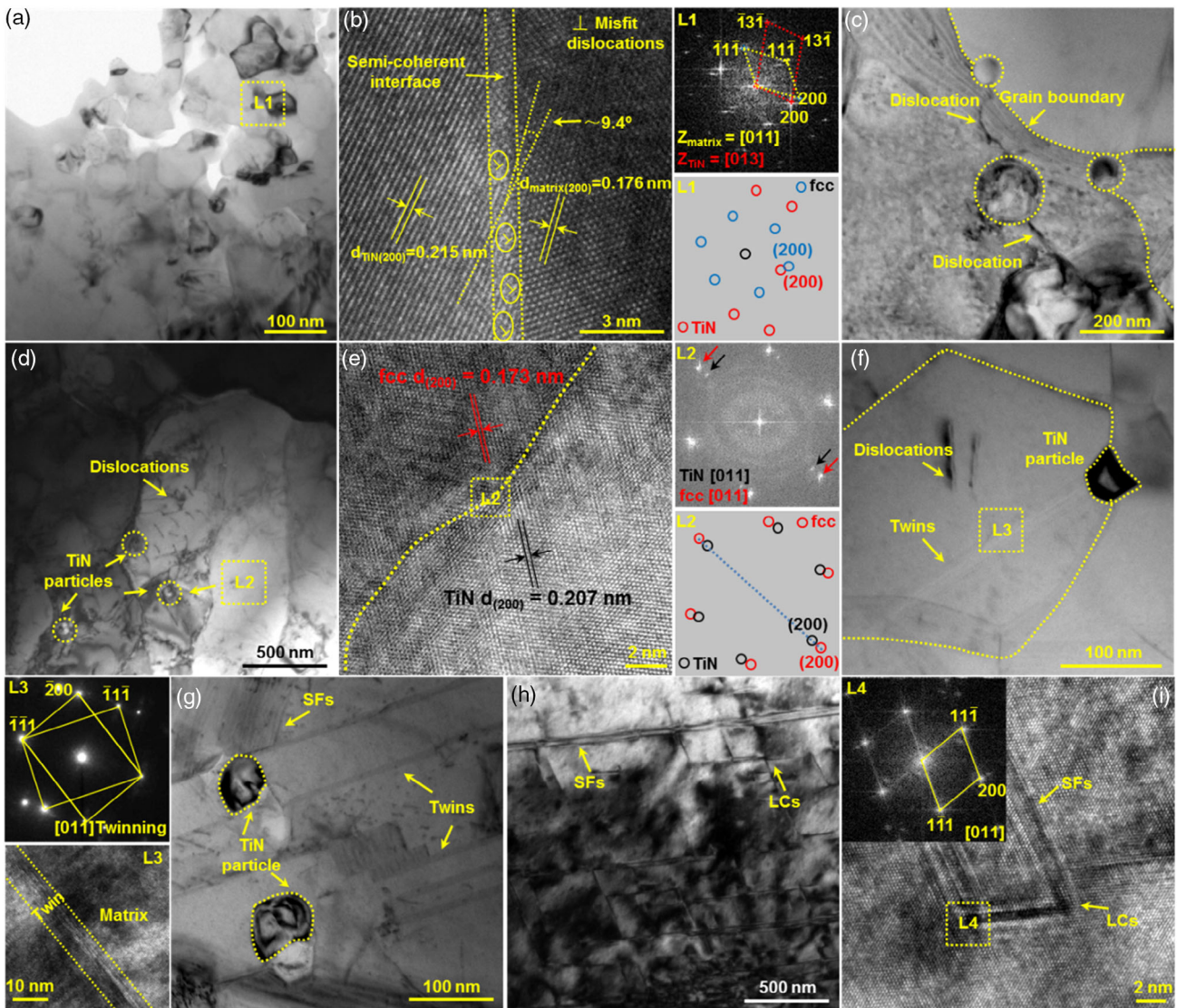
2200939 (4 of 7)

Figure 6. a,b) Detailed microstructural analysis at the grip of tensile CoCrNi/TiN composites annealed at 700 °C for 1 h. (a) BFTEM micrograph of the grip of tensile CoCrNi/TiN composites. (b) HRTEM image and SAED pattern (L1) indicating the orientation relationship between fcc and TiN phases. c–i) Detailed microstructural analysis of the tip of tensile CoCrNi/TiN composites annealed at 700 °C for 1 h. (c) BFTEM image implies the interaction between high-density nanosize TiN particles with dislocations. (d) The high-density intragranular dislocations. (e) HRTEM image and SAED pattern (L2) showing the interface between fcc and TiN phases. (f) BFTEM images showing the interaction between nanotwins and TiN particle distributed at grain boundary. (g) the TiN particles embedded in the nanotwins. (h) BFTEM image and (i) HRTEM image indicating the formation of SFs and LCs.

be also initiated by the high stress concentration, and the nanotwins with a large thickness-length ratio have a positive influence in ductile fracture via serving as an energetic energy-dissipating mechanism, which favors the improvement in fracture toughness.[38,39]

Furthermore, the interacted SFs were detected in the composites, resulting in the formation of LCs, as indicated in the TEM image of Figure 6h and HRTEM image of Figure 6i. The high number density of SFs can benefit strain hardening by acting as a barrier to impede the propagation of dislocations and deliver the dynamic Hall–Petch effect.[40–43] Also, like the SFs, dislocations from four directions can be pinned by the LC locks, and other

dislocations are hard to move near the LC locks, then causing dislocation pile-up,[42] which has a positive influence in the strengthening and strain hardening of MEAs/high-entropy alloys.[43–45]

From the evidence obtained from above analysis, the refined grains, the interaction between dislocations and TiN nanoparticles, and the SFs and LCs are responsible for relatively higher yield strength (0.77 GPa). On the other hand, the formation of nanotwins, the interaction between nanotwin and TiN particles, and the concurrent process of GBS and the accommodation from intragranular dislocation in the softer fcc matrix come together to contribute to the excellent ductility (FS of 55.2%).

ADVANCED
SCIENCE NEWS

www.advancedsciencenews.com

ADVANCED
ENGINEERING
MATERIALS

www.aem-journal.com

4. Conclusion

The CoCrNi/TiN composites have been processed using cold rolling and annealing. The optimized processing route has proven to be capable of delivering superior mechanical performance. Under the as-SPSed condition, the CoCrNi/TiN composites exhibited the fracture strain of 41.9%, YS of 0.48 GPa, UTS of 0.88 GPa, and hardness of 232.0 Hv. After rolling at 25 °C for the thickness reduction of 50%, the alloy presented the fracture strain of 6.9%, YS of 1.24 GPa, UTS of 1.41 GPa, and hardness (408.9 Hv). After rolling at 25 °C for the thickness reduction of 50%, and annealing at 700 °C for 1 h, a good combination of yield strength of 0.77 GPa, UTS of 1.01 GPa, and FS of 55.2% could be obtained in the samples. The superior strength–ductility synergy stems from the refined structure, the formation of lattices defects (i.e., SFs and LCs), the interaction of nanotwin–TiN particles, and the concurrent process of potential GBS accommodated by intragranular dislocation in the softer fcc matrix.

Conflict of Interest

The authors declare no conflict of interest.

Data Availability Statement

The data that support the findings of this study are openly available in [National Key Research and Development Program of China] at [https://doi.org/10.1002/adem.202200939], reference number [52071343].

[1] M. Yang, D. Yan, F. Yuan, P. Jiang, E. Ma, X. Wu, *Proc. Natl. Acad. Sci.* **2018**, *115*, 7224.
[2] Y. Ma, F. Yuan, M. Yang, P. Jiang, E. Ma, X. Wu, *Acta Mater.* **2018**, *148*, 407.
[3] H. Huang, J. Y. Wang, H. L. Yang, S. X. Ji, H. L. Yu, Z. L. Liu, *Scr. Mater.* **2020**, *188*, 216.
[4] S. Praveen, J. W. Bae, P. Asghari-Rad, J. M. Park, H. S. Kim, *Mater. Sci. Eng., A* **2018**, *734*, 338.
[5] G. W. Hua, L. C. Zeng, H. Du, X. W. Liu, Y. Wu, P. Gong, Z. T. Fan, Q. Hu, E. P. George, *J. Mater. Sci. Technol.* **2020**, *54*, 196.
[6] B. Gludovatz, A. Hohenwarter, K. V. S. Thurston, H. Bei, Z. Wu, E. P. George, R. O. Ritchie, *Nat. Commun.* **2016**, *7*, 10602.
[7] J. B. Li, B. Gao, Y. T. Wang, X. H. Chen, Y. C. Xin, S. Tang, B. Liu, Y. Liu, M. Song, *J. Alloys Compd.* **2019**, *792*, 170.
[8] J. B. Seol, J. W. Bae, J. G. Kim, H. Sung, Z. M. Li, H. H. Lee, S. H. Shim, J. H. Jang, W. S. Ko, S. I. Hong, H. S. Kim, *Acta Mater.* **2020**, *194*, 366.
[9] J. Y. Wang, H. L. Yang, H. Huang, J. M. Ruan, S. Ji, *J. Alloys Compd.* **2019**, *798*, 576.
[10] D. Lee, M. P. Agustianingrum, N. Park, N. Tsuji, *J. Alloys Compd.* **2019**, *800*, 372.
[11] J. P. Liu, J. X. Chen, T. W. Liu, C. Li, Y. Chen, L. H. Dai, *Scr. Mater.* **2020**, *181*, 19.
[12] S. Yoshida, T. Bhattacharjee, Y. Bai, N. Tsuji, *Scr. Mater.* **2017**, *134*, 33.
[13] X. W. Liu, G. Laplanche, A. Kostka, S. G. Fries, J. Pfetzing-Micklich, G. Liu, E. P. George, *J. Alloys Compd.* **2019**, *775*, 1068.
[14] B. Gludovatz, A. Hohenwarter, D. Catoor, E. H. Chang, E. P. George, R. O. Ritchie, *Science* **2014**, *345*, 1153.
[15] Y. Deng, C. C. Tasan, K. G. Pradeep, H. Springer, A. Kostka, D. Raabe, *Acta Mater.* **2015**, *94*, 124.
[16] Y. L. Zhao, T. Yang, Y. Tong, J. Wang, J. H. Luan, Z. B. Jiao, D. Chen, Y. Yang, A. Hu, C. T. Liu, J. J. Kai, *Acta Mater.* **2017**, *138*, 72.
[17] K. S. Ming, W. J. Lu, Z. M. Li, X. F. Bi, J. Wang, *Acta Mater.* **2020**, *188*, 354.
[18] R. P. Zhang, S. T. Zhao, J. Ding, Y. Chong, T. Jia, C. Ophus, M. Asta, R. O. Ritchie, A. M. Minor, *Nature* **2020**, *581*, 283.
[19] Ł. Rogal, D. Kalita, A. Tarasek, P. Bobrowski, F. Czerwinski, *J. Alloys Compd.* **2017**, *708*, 344.
[20] J. Y. Wang, H. L. Yang, Z. L. Liu, S. X. Ji, R. D. Li, J. M. Ruan, *J. Alloys Compd.* **2019**, *772*, 272.
[21] E. P. George, D. Raabe, R. O. Ritchie, *Nat. Rev. Mater.* **2019**, *4*, 515.
[22] H. C. Pan, R. Kang, J. R. Li, H. B. Xie, Z. R. Zeng, Q. Y. Huang, C. L. Yang, Y. P. Ren, G. W. Qin, *Acta Mater.* **2020**, *186*, 278.
[23] R. B. Chang, W. Fang, H. Y. Yu, X. Bai, X. Zhang, B. X. Liu, F. X. Yin, *Scr. Mater.* **2019**, *172*, 144.
[24] R. X. Zheng, M. W. Liu, Z. Zhang, K. Ameyama, C. L. Ma, *Scr. Mater.* **2019**, *169*, 76.
[25] H. Hadraba, Z. Chlup, A. Dlouhy, F. Dobes, P. Roupcova, M. Vilemova, J. Matejicek, *Mater. Sci. Eng., A* **2017**, *689*, 252.
[26] Q. Y. Tan, J. Q. Zhang, Q. Sun, Z. Q. Fan, G. Li, Y. Yin, Y. G. Liu, M. X. Zhang, *Acta Mater.* **2020**, *196*, 1.
[27] B. G. Park, A. G. Grosky, A. K. Hellier, *Composites, Part B* **2008**, *39*, 1270.
[28] S. Jiang, H. Wang, Y. Wu, X. Liu, H. Chen, M. Yao, B. Gault, D. Ponge, D. Raabe, A. Hirata, M. Chen, Y. Wang, Z. Lu, *Nature* **2017**, *544*, 460.
[29] N. Li, H. Wang, A. Misra, J. Wang, *Sci. Rep.* **2014**, *4*, 6633.
[30] N. T. Nguyen, P. Asghari-Rad, P. Sathiyamoorthi, A. Zargaran, C. S. Lee, H. S. Kim, *Nat. Commun.* **2020**, *11*, 2736.
[31] T. Yang, Y. L. Zhao, Y. Tong, Z. B. Jiao, J. Wei, J. X. Cai, X. D. Han, D. Chen, A. Hu, J. J. Kai, K. Lu, Y. Liu, C. T. Liu, *Nature* **2018**, *362*, 933.
[32] I. Moravcik, L. Gouvea, J. Cupera, I. Dlouhy, *J. Alloys Compd.* **2018**, *748*, 979.
[33] C. F. Sun, P. P. Li, S. Q. Xi, Y. Zhou, S. W. Li, X. G. Yang, *Mater. Sci. Eng., A* **2018**, *728*, 144.
[34] J. Chen, P. Y. Niu, T. Wei, L. Hao, Y. Z. Liu, X. H. Wang, *J. Alloys Compd.* **2015**, *649*, 630.
[35] S. Lu, J. Agran, L. Vitos, *Acta Mater.* **2018**, *156*, 20.
[36] T. G. Langdon, *J. Mater. Sci.* **2009**, *44*, 5998.
[37] C. Liu, P. Shanthraj, J. D. Robson, M. Diehl, S. Dong, J. Dong, W. Ding, *Acta Mater.* **2019**, *178*, 146.
[38] Y. N. Wang, C. Xie, Q. H. Fang, X. Liu, M. H. Zhang, Y. W. Liu, L. X. Li, *Int. J. Solids Struct.* **2016**, *102*, 230.

**ADVANCED
SCIENCE NEWS**

www.advancedsciencenews.com

**ADVANCED
ENGINEERING
MATERIALS**

www.aem-journal.com

[39] T. W. He, M. L. Feng, X. H. Chen, *Math. Mech. Solids* **2018**, *24*, 1243.

[40] W. Wu, S. Ni, Y. Liu, B. Liu, M. Song, *Mater. Charact.* **2017**, *127*, 111.

[41] X. L. Wu, Y. T. Zhu, Y. G. Wei, Q. Wei, *Phys. Rev. Lett.* **2009**, *103*, 205504.

[42] L. Dupuy, M. C. Fivel, *Acta Mater.* **2002**, *50*, 4873.

[43] J. Y. Wang, H. L. Yang, H. Huang, J. P. Zou, S. X. Ji, Z. L. Liu, *Mater. Sci. Eng., A* **2020**, *796*, 139974.

[44] L. Zhang, Z. H. Hu, L. Zhang, H. Wang, J. B. Li, Z. Li, J. X. Yu, B. L. Wu, *Scr. Mater.* **2022**, *211*, 114497.

[45] K. Jiang, T. F. Ren, G. B. Shan, T. Ye, L. Y. Chen, C. X. Wang, F. Zhao, J. G. Li, T. Suo, *Mater. Sci. Eng., A* **2020**, *797*, 140125.